Effective Suppressing Phase Segregation of Mixed-Halide Perovskite by Glassy Metal-Organic Frameworks

Mehri Ghasemi, Xuemei Li, Cheng Tang, Qi Li, Junlin Lu, Aijun Du, Jaeho Lee, Dominique Appadoo, Luiz H. G. Tizei, Sang T. Pham, Lianzhou Wang, Sean M. Collins, Jingwei Hou,* Baohua Jia,* and Xiaoming Wen*

Lead mixed-halide perovskites offer tunable bandgaps for optoelectronic applications, but illumination-induced phase segregation can quickly lead to changes in their crystal structure, bandgaps, and optoelectronic properties, especially for the Br–I mixed system because CsPbI3 tends to form a non-perovskite phase under ambient conditions. These behaviors can impact their performance in practical applications. By embedding such mixed-halide perovskites in a glassy metal-organic framework, a family of stable nanocomposites with tunable emission is created. Combining cathodoluminescence with elemental mapping under a transmission electron microscope, this research identifies a direct relationship between the halide composition and emission energy at the nanoscale. The composite effectively inhibits halide ion migration, and consequently, phase segregation even under high-energy illumination. The detailed mechanism, studied using a combination of spectroscopic characterizations and theoretical modeling, shows that the interfacial binding, instead of the nanoconfinement effect, is the main contributor to the inhibition of phase segregation. These findings pave the way to suppress the phase segregation in mixed-halide perovskites toward stable and high-performance optoelectronics.

1. Introduction

In recent years, lead (Pb)-based metal-halide perovskites (MHPs) with the chemical formula ABX3 (A = $CH_3NH_3^+$ (MA^+), $CH(NH_2)_2^+$ (FA^+), or Cs+; B = Pb2+; and X = Br^-, Cl^-, I^-, or mixtures thereof) have been intensively studied for optoelectronic applications.[1] Compositional tuning enables this family of materials to display different optoelectronic features sought after for light-emitting diodes (LEDs), solar cells, and detectors.[2] Such tunability can be achieved through the mixing of either A-site cations,[3] B-site metal cations of Pb^{2+}, Sn^{2+}, and Bi^{3+},[3c,4] and particularly X-site halides (X = Br^-, Cl^-, I^-).[5] Mixed-ion perovskites are currently featuring the most efficient and versatile optoelectronic devices.[6] By adjusting the ratio of the anionic component of halides (Br^-, Cl^-, I^-), the bandgap of MHPs can be readily tuned across the whole visible light spectrum.[7] Therefore,

M. Ghasemi, B. Jia, X. Wen
School of Science
RMIT University
Melbourne, VIC 3000, Australia
E-mail: baohua.jia@rmit.edu.au; xiaoming.wen@rmit.edu.au
X. Li, J. Lee, L. Wang, J. Hou
School of Chemical Engineering
The University of Queensland
St. Lucia, QLD 4072, Australia
E-mail: jingwei.hou@uq.edu.au
C. Tang, A. Du
School of Chemistry and Physics
Centre for Materials Science
Queensland University of Technology
2 George St, Brisbane City, QLD 4001, Australia

Q. Li, J. Lu
Centre for Translational Atomaterials
Swinburne University of Technology
Hawthorn, VIC 3122, Australia
D. Appadoo
Australian Synchrotron
800 Blackburn Rd, Clayton, VIC 3168, Australia
L. H. G. Tizei
Université Paris-Saclay, CNRS
Laboratoire de Physique des Solides
91405 Orsay, France
S. T. Pham, S. M. Collins
Bragg Centre for Materials Research
School of Chemical and Process Engineering and School of Chemistry
University of Leeds
LS2 9JT Leeds, UK
L. Wang
Australian Institute for Bioengineering and Nanotechnology
The University of Queensland
St Lucia, QLD 4072, Australia

The ORCID identification number(s) for the author(s) of this article can be found under https://doi.org/10.1002/smll.202304236

ADVANCED
SCIENCE NEWS
www.advancedsciencenews.com

NANO · MICRO
small
www.small-journal.com

the optical absorption of MHPs can be modulated via bandgap engineering to realize efficient devices like high-efficient LEDs, top-cell tandem solar cells, and lasers.[8] Nevertheless, the instability of these compounds in response to external stimuli, specifically illumination, has a significant impact on their practical use as it negatively impacts the device's lifetime.[9] Under continuous light illumination or with an applied bias, mixed-halide perovskites quickly undergo structural changes that resulted from phase segregation in the system, for example, I-rich domains in Br and I mixed halide MHPs can lead to the formation of the non-perovskite phase as the $CsPbI_3$ favors non-perovskite orthorhombic phase under ambient conditions.[10] Such a behavior deteriorates the optoelectronic characteristics, lower open-circuit voltage (V_{oc}), and leads to poor stability.[9,11] Suppressing the ionic phase segregation has therefore been extensively studied through mixing organic/inorganic A-site cations (MA^+, FA^+, Cs^+),[2a,12] morphology engineering (grain size and film thickness),[10c,13] controlling halide defect density,[10c–e] and interface engineering.[14] For example, by identifying a correlation between the carrier diffusion length and the segregation rate, it has been determined that nanoparticle size is effective at suppressing phase segregation. For $CsPbI_{1.5}Br_{1.5}$ based film has a threshold crystal size of 46 ± 7 nm, below which the phase segregation can be mitigated albeit at a mild illumination condition of 60 mW cm^{-2} light intensity.[10c,15] However, most of these techniques are non-trivial and scaling-up can be challenging. A deeper understanding of the phase segregation process, and providing a practical method to suppress the undesirable effect are essential for ensuring the optoelectronic devices with long-term stability.

Embedding MHPs into a substrate is a feasible method for enhancing their stability. Polymers, inorganic zeolites and glasses, and recently metal-organic frameworks (MOFs) have been studied.[16] Among them, MOFs are organic–inorganic hybrid compounds formed by coordination bonds between organic ligands and metal ions. Their high tunable structure and chemical properties make them a promising candidate for hosting MHPs.[17] However, the pores of crystalline MOF are typically too small to accommodate MHPs, necessitating strategic structural tailoring.[18] The recent discovery of the meltable, glassy, and amorphous MOFs offers unique opportunities for MHP/MOF composites, where the viscous flowing MOF liquid at a high temperature can facilitate the interfacial bonding and shaping of the composite, generating highly processible and stable nanocomposites.[19] This offers a unique opportunity to study the precise interaction between mixed cation MHPs and MOFs and its effect on phase segregation.

In the current work, we develop a family of scalable composites containing $CsPb(Br_{1-x}I_x)_3$ embedded in MOF glass matrix{$Zn[(Im)_{1.95}(bIm)_{0.05})]$, Im: imidazolate; bIm: benzimidazolate}, (denoted as $a_gZIF-62$) matrix through liquid-phase sintering. We have previously demonstrated that the $a_gZIF-62$ matrix can stabilize $CsPbI_3$ nonequilibrium perovskite phases through interfacial interactions, and the matrix is a compatible platform for a range of halide ion compositions.[19] In the present work, we further study the system of the mixed-halide $CsPb(Br_{1-x}I_x)_3$ and $a_gZIF-62$ composites, fabricated from liquid phase sintering. The perovskite component was synthesized through ball milling, resulting in a particle size distribution with a comparatively broad range and posing an additional difficulty for phase stabilization.

The composite features significantly enhanced light emission efficiency over pure perovskite. We further identify the strong correlation between the halide composition and the perovskite emission wavelength at the nanoscale and also reveal the significant passivation of the perovskite surface by $a_gZIF-62$. This surface passivation effectively suppresses the unfavorable phase segregation, even at a considerably high illumination intensity of 500 mW cm^{-2} (relative to 100 mW cm^{-2} excitation intensity equivalent to 1 sun illumination). We combine a theoretical model and spectroscopic technique to fathom the interaction between the mixed-halide perovskite and $a_gZIF-62$, revealing that the chemical interaction at the interface is responsible for the exceptionally high photostability. These findings open new avenues to elevate the stability and the performance of perovskite-based optoelectronic devices, enabling future device applications of mixed halide perovskites.

2. Results and Discussion

2.1. Formation and Structure of Perovskites-ZIF Glass Composites

Samples were fabricated by liquid-phase sintering of $CsPbBr_{1.5}I_{1.5}$ with pre-formed glassy ZIF-62 ($a_gZIF-62$). More details can be found in the Experimental Section. A small number of ZIFs can experience melting at high temperatures, generating microporous glasses after quenching.[20] Their distinct physicochemical properties, including porosity, ductility, optical characteristics, and processibility, have made them unique candidates as matrices for other functional materials.[19,21] In this work, $CsPbBr_{1.5}I_{1.5}$ and ZIF-62 were prepared mechanochemically separately. After melt-quenching the ZIF-62, the formed glassy $a_gZIF-62$ was mixed with 25 wt% of $CsPbBr_{1.5}I_{1.5}$ through another round of brief ball milling. The mixture was sintered at different temperatures from 150 to 350 °C, followed by a quenching step using liquid nitrogen (N_2) under a constant flow of argon (Ar). The resultant component is referred to as $(CsPbBr_{1.5}I_{1.5})_{0.25}(a_gZIF-62)_{0.75}$, where 0.25 and 0.75 represent the weight fraction of each component.

Ex situ X-ray Diffraction (XRD) patterns showed wide peaks at $\approx15°$ and $30°$ for composites prepared at 150 °C (**Figure 1**a and Figure S1, Supporting Information). We attribute these diffuse features to $a_gZIF-62$.[19] Peaks associated with the crystalline perovskite structure gradually emerged along with higher sintering temperatures,[19,22] indicating the high-temperature treatment is beneficial for the formation of the crystal structures.[23] No identifiable peak shift was observed in the XRD patterns of the composites, indicating a relatively minor strain effect for the crystalline phase within the composite. Higher sintering temperature reduced the full width at half maximum (FWHM) of the XRD peaks (Figure S1b, Supporting Information), which can be ascribed to the increase of the perovskite nanoparticle size. With the Debye–Scherrer method, the average $CsPbBr_{1.5}I_{1.5}$ crystallite size can be retrieved (Figure 1b), which increased from ≈6 to 17 nm when the sintering temperature raised from 250 to 350 °C. This observation is consistent with our previous findings.[19] No diffraction peak associated with PbX_2 (X: Br or I) was detected. In addition, it is noteworthy that the optoelectronically active crystal phases are well preserved in these composites, while thermodynamic
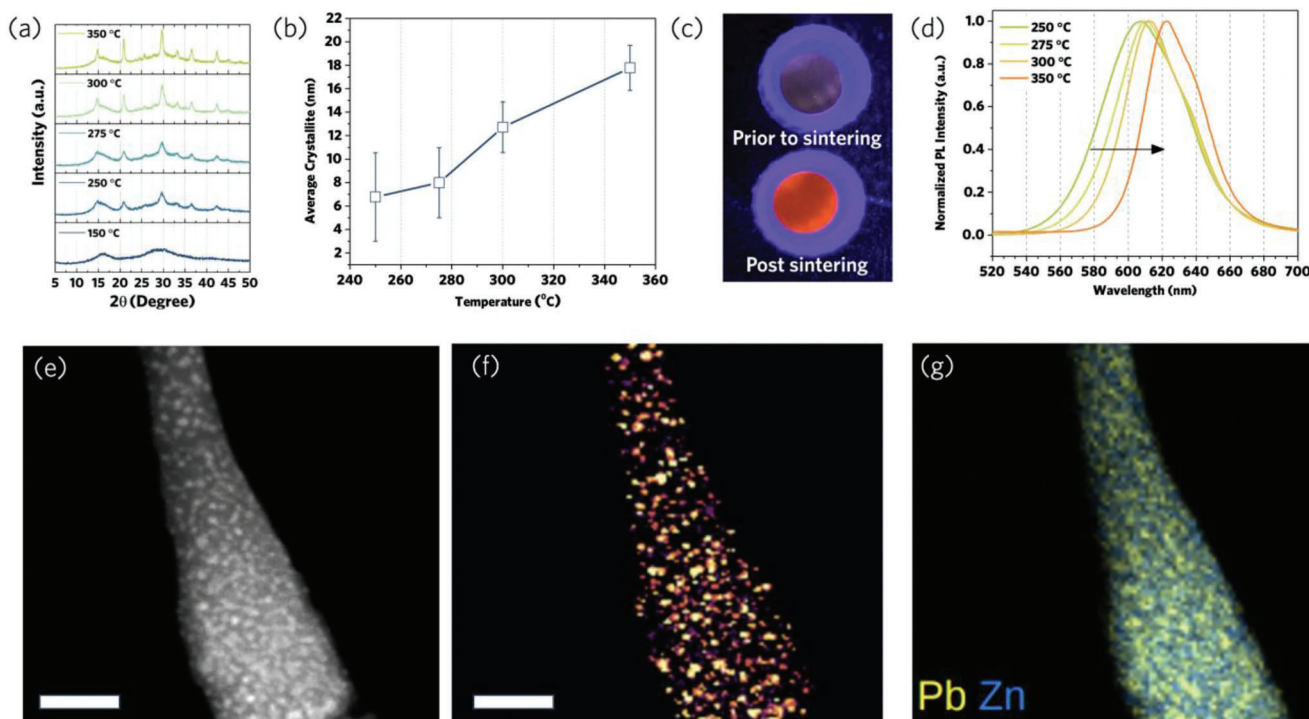
Figure 1. a) XRD patterns of $(CsPbBr_{1.5}I_{1.5})_{0.25}(a_gZIF-62)_{0.75}$ composites sintered at different temperatures. b) Average sizes of $CsPbBr_{1.5}I_{1.5}$ NCs deconvoluted from ex situ powder XRD. c) Optical image of the sample prior to and after 275 °C sintering. Image taken under 365 nm UV irradiation. d) Photoluminescence (PL) spectra for $(CsPbBr_{1.5}I_{1.5})_{0.25}(a_gZIF-62)_{0.75}$ composites prepared with different sintering temperatures. e) ADF-STEM image and the corresponding f) SED-STEM mapping and g) EDS-STEM mapping of the composite sintered at 300 °C.

factors may promote the transformation of $CsPbX_3$ perovskites from active phases (α, β, and γ) to inactive orthorhombic phase (δ), particularly for the pure $CsPbI_3$.[24] The composite, therefore, showed characteristic emission in the orange wavelength region after sintering (Figure 1c,d). The red shift with higher sintering temperature should be attributed to the increased crystalline size, which led to a reduced quantum confinement effect.[19] It should be noted that samples only containing pure $CsPbBr_{1.5}I_{1.5}$ crystallite powders showed negligible light emission even after identical sintering treatment (results not shown). In addition, the sample prior to sintering also had very weak orange light emission (Figure 1c), indicating the effective defect passivation through the compositing and sintering process.

We further performed the scanning electron microscope (SEM) to examine the microstructure and phase distribution within the composites. Based on the combination of the secondary electron and backscattering images (Figure S2, Supporting Information), the perovskite and MOF glass showed clear phase contrast, and the distribution of the particles was relatively even. An increase in the sintering temperature rendered the composite surface to be smoother, due to the remelting of the glass phase and the viscous flowing states.

Annular dark-field-scanning transmission electron microscopy (ADF-STEM) images showed that the mixed-halide perovskite was evenly embedded in the $a_gZIF-62$ matrix (Figure 1e–g and Figure S3, Supporting Information) despite only brief ball milling being applied for homogenization, and the elemental mapping further corroborated the expected phase distributions. In addition, we applied scanning electron diffraction (SED) to

confirm the distribution of the crystalline phase. By plotting the number of Bragg diffraction disks detected at each probe position, we can co-locate the crystalline fraction with the MHP elementals signatures (Figure 1f,g). The crystalline maps derived from the SED further confirmed the homogeneous distribution of the crystalline phases with an average particle size of $\approx$10 nm.[19]

Cathodoluminescence (CL)-STEM can provide key information on the composite emission profile at a nanoscale. Focused ion beam (FIB) milling was performed for the CL-STEM sample preparation, to extract a $\approx$10 nm thick lamella to expose individual perovskite grains along the direction of the electron probe. CL from composites has emission peaks centered at around 620 nm (**Figure 2** and Figures S4 and S5, Supporting Information). The precise emission spectra varied (Figure 2) and Gaussian-fitted maps of CL hyperspectral datasets showed that this was due to interparticle variations (Figure S4, Supporting Information). Histograms of the fitted coefficients from a large ensemble of particles (Figure S5, Supporting Information) showed that the emission peak center varied from 610 to 690 nm, with a main contribution at $\approx$620 nm and two other visible contributions at $\approx$635 and 655 nm. 2D histograms of amplitude versus the center of the fitted Gaussians (Figure S5, Supporting Information) showed a good correlation.

Correlating the mixed halide perovskite's composition and emission characteristics has been studied mostly in their bulk phases. This work tried to establish this correlation at a nanoscale. The CL emission spectra were overlaid with the ADF-STEM with simultaneous EDS results. Five separate areas were
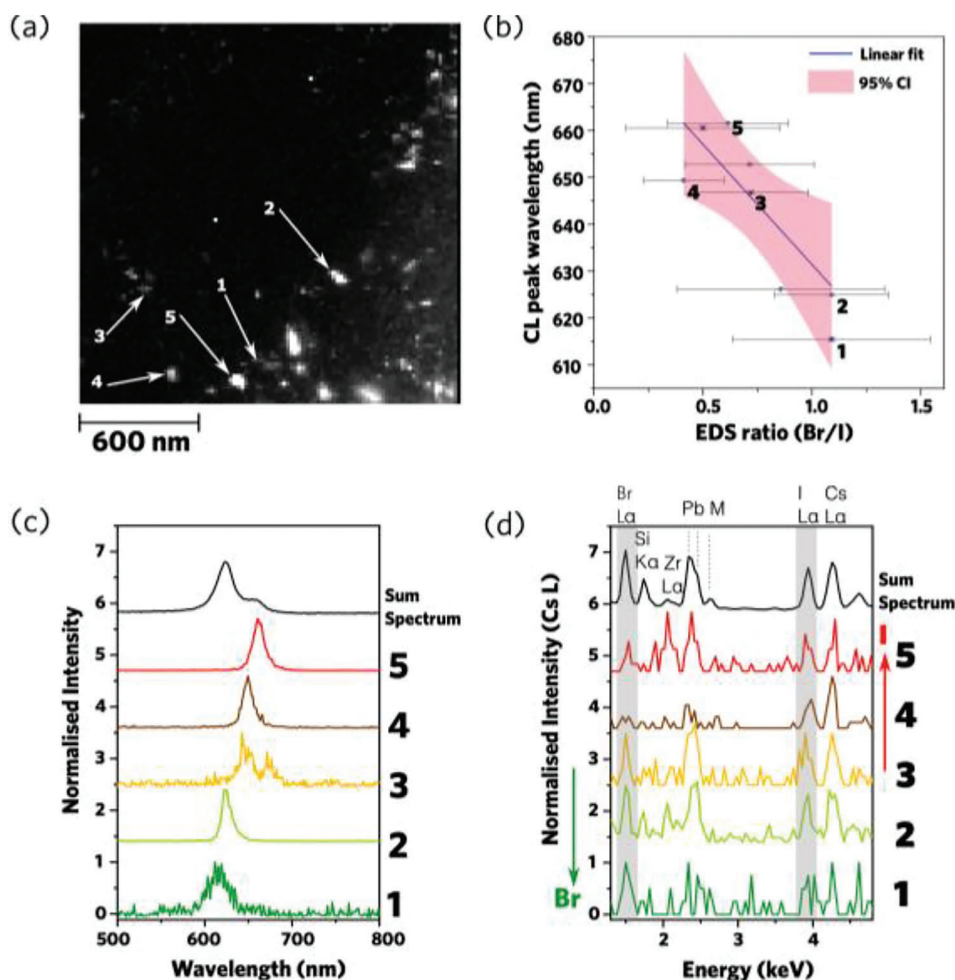
Figure 2. Correlative measurements by STEM-CL and STEM-EDS measurement of $(CsPbBr_{1.5}I_{1.5})_{0.25}(a_gZIF-62)_{0.75}$ composite sintered at 300 °C. a) Panchromatic STEM-CL image. Arrows mark grains used reference points for registration of CL and EDS signals (Figure S6, Supporting Information). b) Correlation of the peak emission wavelength and Br/I ratio for eight grains in the overlapping window of the two independent scans (separate microscopes). Error bars show the propagated uncertainty from counts in each energy window for the Br/I ratio (see Experimental Section) and the standard error in the Gaussian center fit to the emission peak. A linear fit and 95% confidence interval (CI) are also overlaid. Example c) CL spectra and d) EDS spectra illustrate the trend, also showing spectra with contributions from multiple overlapping grains (position 3).

identified from the overlay, and their corresponding CL and EDS spectra were presented (Figure 2 and Figure S6, Supporting Information). The correlated CL peak maximum from Gaussian fitting showed almost linear fitting with a 95% confidence interval (CI), being statistically significant averages for the particles presented in the field of view. Area 3 had two contributing CL peaks, possibly because the position contained contributions from more than one grain in CL and EDS. Still, these results confirmed the relationship between the alloyed composition and their emission profile at a nanoscale. It should be noted that FIB can lead to perovskite damage and quenching of light emission. However, the distinct CL emission for individual grains, particularly for grains 2 and 5 both sitting on a step in the milling process, confirmed the stability of the composite under sample preparation and examination conditions. The stability of the composite is further substantiated by the similar peak profile between bulk PL on pellet samples (measured under ambient conditions) and CL on FIB trimmed samples (mea-

sured at ≈170 K, where more significant peak narrowing was identified).

2.2. Photophysical Features of Perovskites-ZIF Glass Composites

As shown in Figure 1d and Figure S7, Supporting Information, the PL characteristics of the as-prepared $(CsPbBr_{1.5}I_{1.5})_{0.25}(a_gZIF-62)_{0.75}$ composites varied based on the sintering temperature. The $(CsPbBr_{1.5}I_{1.5})_{0.25}(a_gZIF-62)_{0.75}$ composites sintered at low temperatures (150 and 175 °C) exhibited weak emission with broad spectra spanning from 450 to around 700 nm (Figure S8, Supporting Information). This emission likely originates from the host $a_gZIF-62$, indicating that the low sintering temperatures of 150 and 175 °C were insufficient for the formation of the perovskite structure or the passivation of surface trap states.[19] This behavior is consistent with the poor crystallinity observed when the sintering temperature is low, where the presence of strong
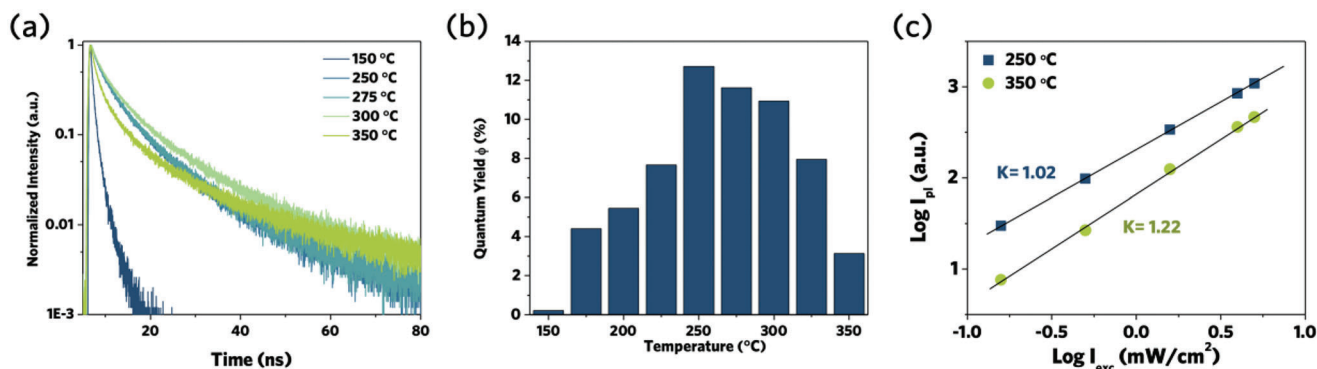
**ADVANCED
SCIENCE NEWS**

www.advancedsciencenews.com

**NANO · MICRO
small**

www.small-journal.com

Figure 3. a) Time-resolved photoluminescence (TRPL) spectra, b) photoluminescence quantum yield (PLQY), and c) PL intensity as a function of excitation intensity for $(CsPbBr_{1.5}I_{1.5})_{0.25}(a_gZIF\text{-}62)_{0.75}$ composites prepared with different sintering temperatures. Under illumination conditions of the $\lambda_{exc} = 405$ nm ($I_{exc} = 500$ mW cm^{-2}).

surface/defect trapping leads to significant nonradiative recombination thus PL quenching. Tracking the PL FWHM for various sintering temperatures (Figure S9, Supporting Information) demonstrated that the PL bandwidth decreased with higher sintering temperatures. In agreement with the XRD results, decreased PL FWHM suggested increased perovskite nanoparticle size, with enhanced size uniformity and homogeneity. The PL intensity increased with sintering temperature, reaching its maximum at 275 °C, and then steadily declined as the temperature rose to 300 and 350 °C (Figure S7a, Supporting Information). Specifically, with the increase in sintering temperature, the PL peak also experienced redshifts, corroborating the increased particle size. These observations indicated that moderate sintering can sufficiently passivate the perovskite defects, while the high temperature may lead to partial decomposition, creating a high density of the non-radiative recombination centers.[25]

To gain a comprehensive understanding of carrier trapping dynamics, we measured time-resolved photoluminescence (TRPL) by time-correlated single photon counting (TCSPC) technique with excitation at 405 nm. **Figure 3**a depicts the PL decay curves of the $(CsPbBr_{1.5}I_{1.5})_{0.25}(a_gZIF\text{-}62)_{0.75}$ composites sintered at different temperatures. The PL decay curves can be well fitted by a bi-exponential fitting of $\gamma = A_1\exp(t/\tau_1) + A_2\exp(t/\tau_2)$, where τ_1 and τ_2 are time constants of the fast and slow components. Effective lifetimes can be obtained by $\tau_{eff} = (A_1\tau_1 + A_2\tau_2)/(A_1 + A_2)$, as listed in Table S1, Supporting Information. At both low (150 °C) and high (350 °C) sintering temperatures, significant fast decay components were observed, which can be ascribed to increased defect trapping at the interface of perovskite and glass (Table S1, Supporting Information). In comparison, such a fast decay component was less significant for the moderate sintering temperatures of 250 and 275 °C. The long lifetime at moderate sintering temperatures can be attributed to the effective passivation of interfacial trap states. These observations were well supported by the PL FWHM and PL intensity variation. Furthermore, the temperature-evolution of PL quantum yield (PLQY) (Figure 3b) of the composites confirmed the highest PLQY values appeared in samples sintered at 250 °C. It should be noted that the PLQY was collected with a relatively high excitation energy (405 nm or 3.06 eV), where the value can approach unity with a lower excitation energy as demonstrated in our previous work.[19]

The PLQY for the pure $CsPbBr_{1.5}I_{1.5}$ was non-detectable even after identical sintering like the composites. Power-dependent PL measurement can be used to assess the nature of carrier recombination in $(CsPbBr_{1.5}I_{1.5})_{0.25}(a_gZIF\text{-}62)_{0.75}$ composites.[26] The PL intensity (I_{PL}) is expressed as a function of excitation intensity I_{exc}: $I_{PL} = I_{exc}^K$, where K is the power index extracted from the slope in a log-log plot (Figure 3c and Figure S10, Supporting Information).[27] The K factor for exciton recombination is approximately equal to 1 ($K \approx 1$) for the benchmark light emission process. It would be greater than 1 for free carriers when bimolecular recombination is quadratic to the excitation.[28] Interestingly, the slope of log I_{PL} against log I_{exc} was equal to 1 for the composites sintered at the temperatures of 250 °C, indicating that excitons were the dominant photogenerated carriers in this group of samples. The excitonic character was attributed to the high exciton binding energy, corresponding to the dynamics of exciton dissociation, and free carrier generation of the perovskites within the composite, given the relatively small particle size and good interfacial contact. In contrast, at high sintering temperatures of 300 and 350 °C, the power index was significantly greater than 1. This suggested that the photogenerated carriers were partly dissociated into free electrons and holes.[29] We hypothesize that with high sintering temperatures, significant exciton dissociation occurred at the interface between the two phases. These observations correlated well with the larger size of the perovskites, decreased PLQY, and increased defect trapping for 300 and 350 °C sintered $(CsPbBr_{1.5}I_{1.5})_{0.25}(a_gZIF\text{-}62)_{0.75}$ samples. Adopting different halide ratios, similar behavior was observed for $(CsPbBrI_2)_{0.25}(a_gZIF\text{-}62)_{0.75}$ composites (Figure S11, Supporting Information), with the highest PLQY of around 14% for the composites achieved with 275 °C sintering.

Figure S12, Supporting Information, demonstrates the contribution of the $a_gZIF\text{-}62$ component in the emission characteristics of the composites sintered at different temperatures. As explained before, for the case of the low sintering temperature of 150 °C, there is no efficient interaction between perovskite and $a_gZIF\text{-}62$; so the PL spectrum exhibits a separate emission with two distinguished peaks (Figure S12a, Supporting Information). Increasing the sintering temperature to a moderate value of 275 °C, the interface of the two phases well prospers, with efficient confinement of the carriers in the perovskite nanocrystals (NCs)
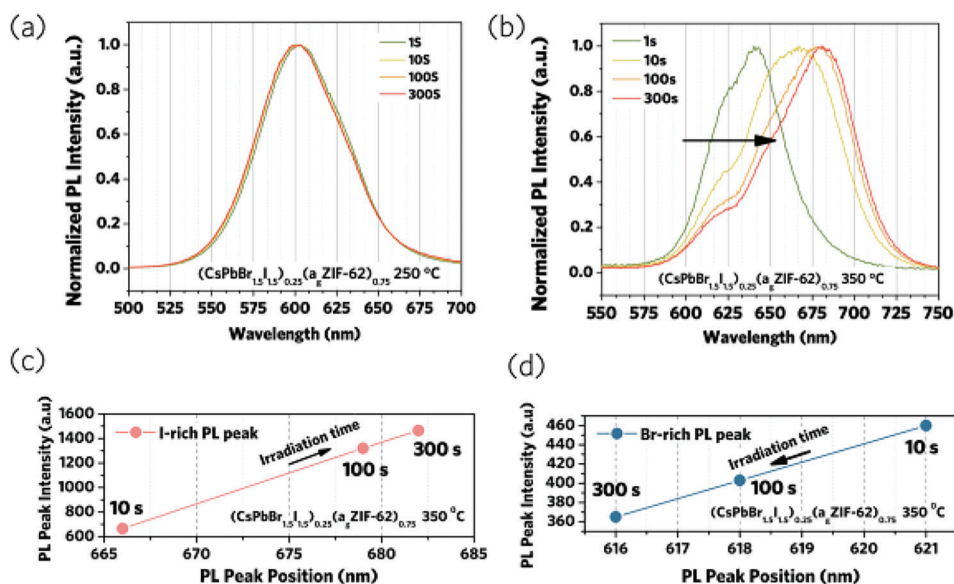
Figure 4. Time evolution of the PL emission spectra of the $(CsPbBr_{1.5}I_{1.5})_{0.25}(a_gZIF-62)_{0.75}$ composites with different sintering temperatures of a) 250 °C, b) 350 °C under λ_{exc} = 405 nm (I_{exc} = 500 mW cm^{-2}). The changes in the c) I-rich and d) Br-rich PL peak positions of the $(CsPbBr_{1.5}I_{1.5})_{0.25}(a_gZIF-62)_{0.75}$ composite sintered at 350 °C.

as the dominant component of the emission, with minor emission from the interface state in the red side, Figure S12b, Supporting Information. In this case, a_gZIF-62 acts as an energy barrier against carrier trapping thus decreasing the energy loss, where the composite works as a whole, instead of two separated phases. Interestingly, a margin shoulder in the long-wavelength side of the PL spectra of this composite can be detected, which is contributed to the emission from the perovskite/a_gZIF-62 interface (Figure S12b, Supporting Information). Further increasing the sintering temperature to 300 °C causes the perovskite particle size enlargement with the following deterioration of the interface interaction, where an increased defect density appears in the interface. This results in increased carrier trapping to the interface state that eventually leads to decreased PLQY of the composite, with more contribution of the PL component from the interface state (Figure S12c, Supporting Information). This highlights that the emission characteristic of the composite is significantly dictated by the extent and quality of the interface interaction of perovskite NC and a_gZIF-62.

2.3. Halide Ion Phase Segregation within the Composites

The halide phase segregation was examined by time-dependent steady-state PL spectra under constant, rather high-energy illumination. **Figure 4** shows a representative time-dependent PL emission from $(CsPbBr_{1.5}I_{1.5})_{0.25}(a_gZIF-62)_{0.75}$ under 405 nm irradiation (I_{exc} = 500 mW cm^{-2}). The complete time-dependent PL spectra of the composites are presented in Figure S13, Supporting Information. For the composites with sintering temperatures of 250 °C, no PL peak splitting was observed even after continuous irradiation over 300 s, indicating an effective suppression of phase segregation (Figure 4a and Figure S15, Supporting Information). In contrast, for the composite sintered at 350 °C, after

10 s of illumination, the PL intensity decreased (Figure S14, Supporting Information), concomitant with a shift in the peak wavelength to longer wavelengths Figure 4b). After 300 s of illumination, two emission peaks were clearly visible at 616 ($\approx$2.0 eV) and 682 nm ($\approx$1.82 eV), whilst the initial peak around 640 nm was quenched.

This predominantly red-shift and minor blue-shift evolution of the PL peaks over continuous irradiation (Figure 4c,d) indicated the formation of phase segregation in the composites, by nucleation of different domains with inhomogeneous halide distribution.[9] The emission peak in the high-energy region was associated with the formation of a Br-rich phase, whereas the emission peak in the low-energy region was attributed to an I-rich phase, with the intensity of the I-rich PL peak increasing significantly upon light illumination (Figure 4c,d). Similar phase segregation has also been observed previously,[30] where the energy transfer between I-rich and Br-rich neighboring atoms causes the I-rich atom with the smaller bandgap to dominate the photoluminescence.[9,31] This is driven by the thermodynamic terms, where the migration of charge carriers to the I-rich phase with a low bandgap can reduce the free energy of the excited system.[32]

Similar behavior was observed for $(CsPbBrI_2)_{0.25}(a_gZIF-62)_{0.75}$ composites (Figure S16, Supporting Information). In the $(CsPbBr_{1.5}I_{1.5})_{0.25}(a_gZIF-62)_{0.75}$ composite the degree of phase segregation was more significant, showing a 16 nm redshift in I-rich PL peak (Figure 4c) than in the $(CsPbBrI_2)_{0.25}(a_gZIF-62)_{0.75}$ composite (6 nm redshift in I-rich PL peak, Figure S16c, Supporting Information) because of the higher amount of Br in the compound. For crystals with greater Br content, the activation energy of 0.17–0.25 eV to promote Br ion migration is lower than for the I ions (0.23–0.45 eV).[9,10e] In general, using high sintering temperatures of 300 and 350 °C, the initial emission peak for the composites was quenched after continuous

ADVANCED
SCIENCE NEWS

www.advancedsciencenews.com

NANO · MICRO
small

www.small-journal.com

illumination, combined with a more dominantly continuous redshift and an increase of PL intensity in the low-energy wavelengths. In contrast, for the composites prepared at moderate sintering temperatures of 250 and 275 °C, the PL peak demonstrated significant tolerance to continuous high-energy illumination, indicating the effective suppression of phase segregation in the $(CsPb(Br_{1-x}I_x)_3)_{0.25}(a_gZIF-62)_{0.75}$ composites.

By tracking the absorption, transient absorption, and photoluminescence profile, previous studies have demonstrated that phase segregation can be a reversible process, where phase segregation happens in tens of seconds, and its recovery takes place on a much longer time scale, such as tens of minutes or hours.[10b,d] Here, we also examined the recovery of the phase segregation samples. After the continuous illumination test, the samples were kept in the dark for 10 min, and the PL spectra were re-measured with short excitation to minimize further excitation influence. Figure S17, Supporting Information, plots the initial, photoinduced, and recovered PL spectra of the 350 °C $(CsPbBr_{1.5}I_{1.5})_{0.25}(a_gZIF-62)_{0.75}$. The PL peak of the composite partially shifted back toward its initial position. This suggests that the effect of phase segregation can be reversible, at least partially, highlighting the remarkable photostability and resistance of these MHP-MOF composite samples to light-induced degradation.

2.4. Mechanism of Phase Segregation Suppressing in Composites

To explain the segregation of halide ions in mixed-halide perovskites, several models based on theoretical and experimental studies have been developed including polaron-assisted halide phase segregation as a result of large electron–phonon coupling[31] and defect-mediated halide ion movement.[13,33] In the case of the former, the free charge carriers deform the surrounding lattice via electron–phonon coupling, and these photogenerated polarons promote more halide migration in the mixed-halide perovskites.[31] If the grain size is smaller than the carrier diffusion length, there is a high probability that the charge carriers are contained within the grains. Unlike large grains whose size exceeds the carrier diffusion length, charge carriers in $CsPb(Br_{1-x}I_x)_3$ can diffuse distances comparable to their own diffusion length with a threshold grain size of 46 nm for $CsPb(Br_{1-x}I_x)_3$.[10c,15] However, the average size of perovskite in our 300 and 350 °C sintered $(CsPbBr_{1.5}I_{1.5})_{0.25}(a_gZIF-62)_{0.75}$ composites was 19 nm (with a relatively large distribution due to ball milling), and the size was even smaller when the sintering temperature was lower, all significantly smaller than the threshold size of 46 nm. Consequently, the size of the perovskite does not offer a satisfactory explanation on its own for the system's different behaviors in transition under illumination.[34] In addition, while factors such as lattice distortion can promote the migration of halide ions, vacancies play a significant role in the formation of stable I-rich and Br-rich domains under prolonged photoirradiation.[10d] To induce phase segregation, halide ion migration is required, and this migration is accelerated along grain boundaries by impurities, vacancies, and dangling bonds.[9,35] Computational analyses indicate that halide defects, specifically halide vacancies and interstitials, contribute to the migration of halide ions by promoting low-energy migration pathways; this defect-assisted halide migration can be triggered by light illumination.[13] Controlling the halide defects can therefore significantly reduce the phase segregation as the facile diffusion pathway for the photoinduced migration of the halides, which has been shown to be sensitive to the synthesis conditions and thermal processing routes.[15,33a]

To investigate the interaction between mixed-halide perovskite and $a_gZIF-62$, first principle theoretical calculations were conducted (see also Experimental Section). Different types of defects were examined in the calculations, including the I/Br vacancy ($V_{I/Br}$), the Pb vacancy (V_{Pb}), I/Br interstitials (I_{Inter}, Br_{Inter}), I/Br_{Pb} and $Pb_{I/Br}$ antisite defects as the potential defects to generate both shallow and deep defect states on the $PbBr_{2-x}I_x$ octahedra termination surfaces. The $a_gZIF-62$ framework can be separated into two different groups with Zn- and imidazole-terminations according to the sequential tetrahedral structures (-Zn-imidazole-Zn-imidazole-) (**Figure 5**a). Therefore, Zn or imidazole groups can be exposed to interact with the mixed-halide perovskite surface (Figure 5b). Absolute values of interaction energies between $a_gZIF-62$ and all types of defects on the surface of the mixed-halide perovskite were relatively high, indicating the high stability of these interactions (Figure 5c) that will suppress the migration of the surface defects.

The imidazole-termination possesses moieties for hydrogen bonding with the surface of the perovskite, while the Zn-termination forms strong Zn- chemical bonding. The difference in charge density indicates strong electron transfer between the surface of $a_gZIF-62$ and perovskite (Figure 5d–g). For imidazole-termination group adsorption, electrons were depleted mostly from the $a_gZIF-62$ and collected on the surface of the perovskite. For Zn-termination group adsorption, the opposite effect was seen. Bader charge analysis showed the 0.67e and 0.86e electrons transfer from imidazole-terminated $a_gZIF-62$ to I/Br_{Pb} and $Pb_{I/Br}$ antisite defective surface, respectively (Figure 5d), and the transfer of 0.26e and 0.35e electrons from the defective surface to the Zn-terminated $a_gZIF-62$, respectively (Figure 5e), comparable to the interaction of the $a_gZIF-62$ surface to interstitial (I_{Inter}, Br_{Inter}) defective perovskite surface (Figure 5f,g). Large absolute values of the interaction energy and large electron transfer emphasize the strong interaction of $a_gZIF-62$ on different defect sites on the surface of the mixed-halide perovskite. The results also suggested that the Zn-termination forms strong chemical bonding with the I^- and Br^- halide ions on the perovskite surface, and the imidazole-termination sites form hydrogen bonding with the perovskite surface. These interactions effectively passivate the ionic defects on the perovskite surface by filling the vacancies ($V_{I/Br}$, V_{Pb}) and bonding to the interstitial (I_{Inter}, Br_{Inter}) and antisite defects ($Pb_{I/Br}$, Br/I_{Pb}), and simultaneously anchor the atoms on the surface of the perovskite structure.

The calculated interfacial bonding was further validated using temperature-resolved in situ synchrotron terahertz (THz) far-infrared (FarIR) vibrational spectroscopy. We investigated the changes in dynamic properties within $(CsPbBr_{1.5}I_{1.5})_{0.25}(a_gZIF-62)_{0.75}$ during the heating and cooling ramp under an Ar environment. The main peaks at 300 and 680 cm^{-1} in **Figure 6**a correspond to the Zn-tetrahedron stretching of ZIF-glass and aromatic ring deformation, respectively.[19] The peak at 300 cm^{-1} experienced an irreversible shift toward lower wavenumbers
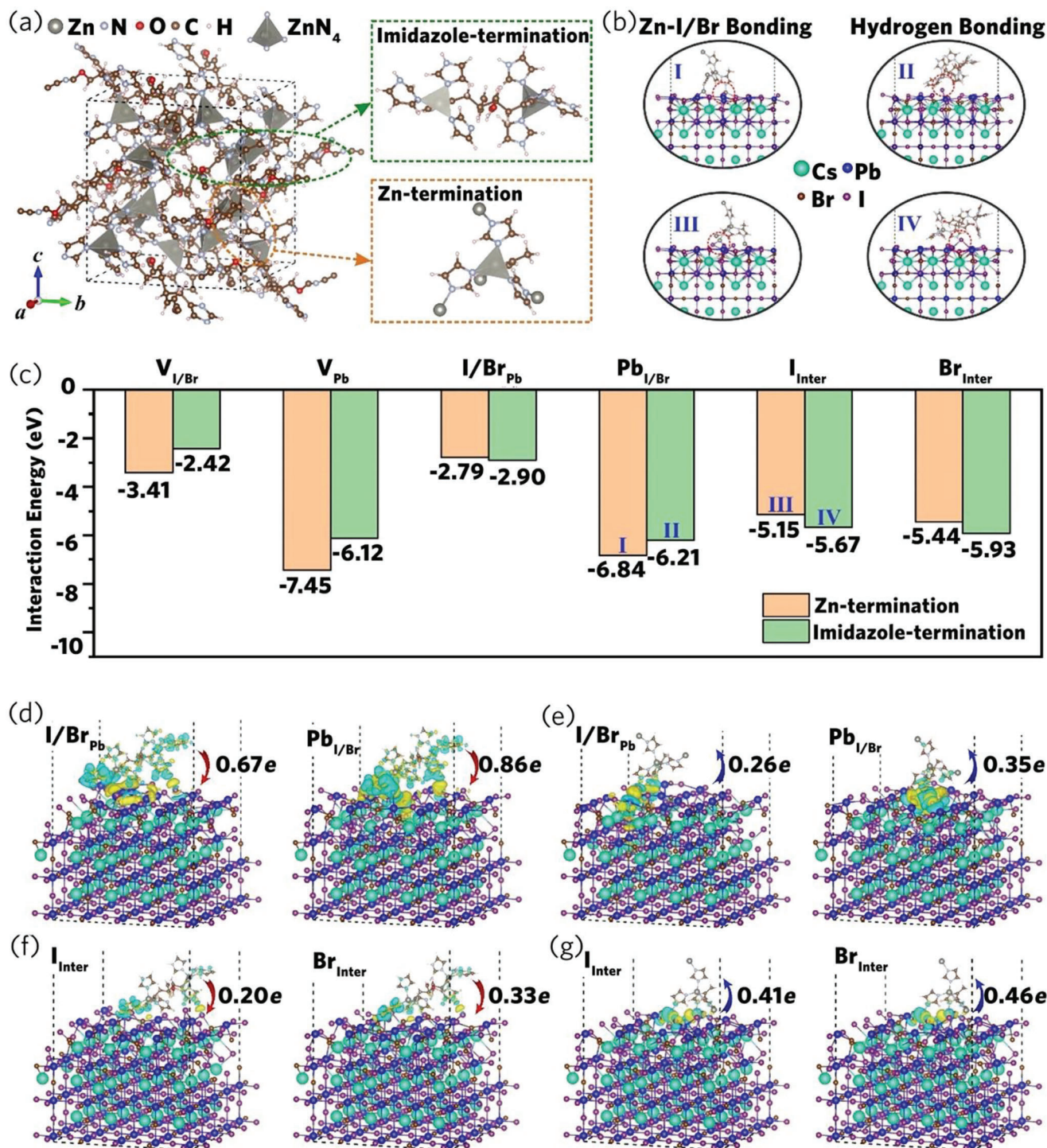
ADVANCED
SCIENCE NEWS

www.advancedsciencenews.com

NANO · MICRO
small
www.small-journal.com

Figure 5. a) Optimized geometry of a_gZIF-62, containing the direct interaction between imidazole and Zn. The imidazole- and Zn-termination group of a_gZIF-62. b) Adsorption behavior for imidazole- and Zn-termination groups adsorbed defective $CsPb(Br_{1-x}I_x)_3$, respectively. (I) and (II) are antisite defects ($Pb_{I/Br}$), (III) and (IV) are I interstitial defects (I/Br_{Inter}). The Zn-termination is strongly bonded with the I or Br atoms of the $CsPb(Br_{1-x}I_x)_3$ surface, while the imidazole-termination exhibits hydrogen bonding. c) Adsorption energies for imidazole- and Zn-termination groups adsorbed defective $CsPb(Br_{1-x}I_x)_3$, respectively. d–g) The charge density difference (iso-value of 0.001 e Å^{-3}) for the adsorption of imidazole- and Zn-terminated a_gZIF-62 on I/Br_{Pb}, $Pb_{I/Br}$, I_{Inter}, and Br_{Inter} defects. Yellow and cyan areas represent electron accumulation and depletion, respectively.
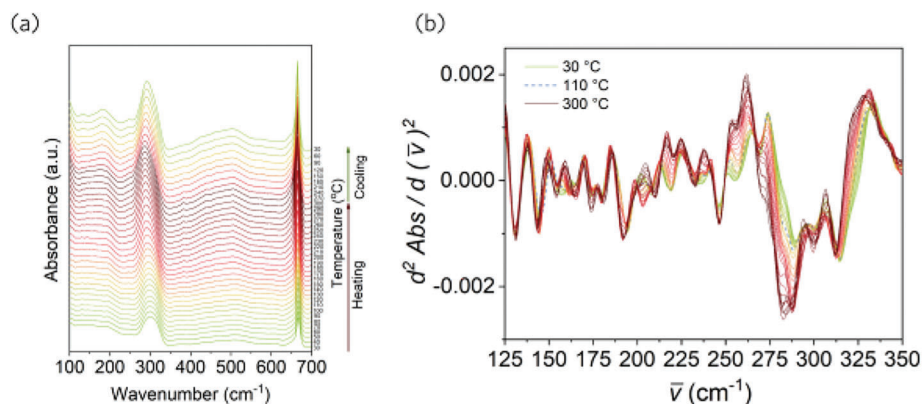
**ADVANCED
SCIENCE NEWS**

www.advancedsciencenews.com

NANO · MICRO

small

www.small-journal.com

Figure 6. a) Temperature-resolved in situ THz FarIR spectra of the $(CsPbBr_{1.5}I_{1.5})_{0.25}(a_gZIF-62)_{0.75}$ composite upon heating to 300 °C and cooling back to room temperature under Ar protection. b) Temperature-resolved second derivative in situ THz FarIR spectra of the $(CsPbBr_{1.5}I_{1.5})_{0.25}(a_gZIF-62)_{0.75}$ composite during the heating ramp. Only three legends of 30, 110, and 300 °C are given for all the curves to guide the eye.

during heating, indicating the formation of interfacial bonds and the variation of Zn—N bonding. The second-derivative spectra revealed the fine vibrational modes of Zn tetrahedra (Figure 6b). Upon heating, new features emerged when the temperature was above ≈200 °C, particularly in the wavenumber of ≈175 and 250 cm^{-1}. These modes can be assigned to Zn-halide stretching and Zn—N vibration within Zn tetrahedron containing both imidazolate and halide ions.[19] This observation aligned with the emergence of the new chemical bonding between the mixed-halide perovskite and $a_gZIF-62$ framework during the heating process. Given negligible weight loss was observed under this temperature (Figure S18, Supporting Information), the possibility of peak shift caused by carbonization can be ruled out.

The enhanced interaction between the halide ions in the perovskite and $a_gZIF-62$ framework can result in a composite with reduced halide vacancies and interstitial, thus lowering the halide ion mobility.[36] This justifies the effective suppression of photoinduced phase segregation in $(CsPbBr_{1.5}I_{1.5})_{0.25}(a_gZIF-62)_{0.75}$ composites sintered at moderate temperatures of 250 and 275 °C.[37] The TRPL and PLQY measurements (Figure 3a,b) also confirmed the suppression of non-radiative recombination loss in composites sintered at 250 and 275 °C, which can be explained by defect passivation at the surface of the perovskite induced by the $a_gZIF-62$ framework. This is consistent with recent findings that light-induced phase segregation can be greatly reduced in $MAPb(Br_xI_{1-x})_3$ perovskite thin films by controlling the defect sites of the halide ions with excess halide ions.[10d] Increasing the sintering temperature to a higher range of 300 and 350 °C may damage the aforementioned binding interactions between the $a_gZIF-62$ and mixed-halide perovskite, resulting in a diminished passivation effect by the $a_gZIF-62$ framework. This is supported by the decrease in PLQY, the quenching of PL, and the increased defect trapping observed in $(CsPbBr_{1.5}I_{1.5})_{0.25}(a_gZIF-62)_{0.75}$ composites prepared at 300 and 350 °C.

3. Conclusions

In this work, we report a family of crystal-glass nanocomposites containing mixed-halide perovskites embedded in $a_gZIF-62$ glass matrices. The resulting composite showed effective suppression of highly undesirable halide phase segregation even in a system

fabricated through ball milling. The collective experimental and computational results reveal that the interfacial contact and bonding between two individual phases are the main contributors to the stabilization effect, through the reduction of halide vacancies and the subsequent inhibition of halide migration. These interactions also passivate the trap states, suppress nonradiative recombination pathways, and enhance the PLQY. Given the highly scalable fabrication process and the highly processible nature, the MOF glass perovskite nanocomposites now serve as key candidates for the development of optoelectronic devices through a layer-by-layer configuration, particularly the mixed cation and anion perovskites for solar panels, where the optimal bandgaps are required for solar spectrum coverage, and LED lighting devices with tunable light emission.

4. Experimental Section

Synthesis of Mixed-Halide Perovskite Nanocrystals of $CsPbBr_{1.5}I_{1.5}$ and $CsPbBrI_2$: All mixed-halide perovskite nanocrystals were synthesized by a mechanochemical process with a total amount of 400 mg precursors, for $CsPbBr_{1.5}I_{1.5}$ and $CsPbBrI_2$ were prepared, with the amount of the of CsBr (65.45 and 42.11 mg), $PbBr_2$ (112.87 and 72.62 mg), CsI (79.90 and 102.82 mg), and PbI_2 (141.78 and 182.45 mg), respectively. 16 g zirconium oxide balls were placed in the ball milling jars. The jars were then set up in the planetary ball milling machine at 800 RPM for 1 h. The powder samples were collected from the jars and stored under ambient conditions for further use.

Synthesis of ZIF-62 and $a_gZIF-62$: ZIF-62 was synthesized by a solvothermal process, which was similar to previous work,[38] with zinc nitrate hexahydrate (1.2 g, 4.00 mmol), imidazole (891 mg, 13.09 mmol), and benzimidazole (16 mg, 0.13 mmol) dissolved in 90 mL of DMF. The solution was then heated in the 100 °C oven for 7 days. After cooling to room temperature, the obtained $[Zn(Im)_{1.95}(bIm)_{0.05}]$ was washed with DMF, followed by twice methanol rinse. The product was then dried in an 80 °C oven overnight before further study.

ZIF-62 glass ($a_gZIF-62$) was fabricated by melting crystalline ZIF-62 in a tube furnace under an Ar atmosphere. The ZIF-62 was heated to 450 °C with a ramping rate of 20 °C, followed by quenching back to room temperature.

Preparation of Perovskites-ZIF Glass Composites: The composites were fabricated by a similar procedure as reported in the previous work.[39] 50 mg mixed halides perovskite was mixed with 150 mg $a_gZIF-62$ by 800 RPM ball milling. After 1 h, the mixture was collected and pelletized into

**ADVANCED
SCIENCE NEWS**

www.advancedsciencenews.com

**NANO · MICRO
small**

www.small-journal.com

round disks. The composite was noted as $(CsPbBr_nI_{3-n})_{0.25}(a_gZIF-62)_{0.75}$, where 0.25 and 0.75 were the mass ratio of perovskites and a_gZIF-62, respectively, n was referred to as the ratio of Br atoms. The disk samples were sintered in a tube furnace and then quenched cryogenically when the temperature reached the designated value.

Steady State and Time-Resolved PL Measurement: The time-dependent steady-state PL spectra were acquired and detected by a QE Pro fluorimeter (Ocean Optics) equipped with a thermoelectrically cooled Si CDD detector. The TRPL was obtained by a TCSPC technique (PicoHarp 300). For the excitation sources, a picosecond diode laser of 405 nm was used with an area of illumination of 7.07 mm^2 (PicoHarp LDH laser) suitably attenuated by a neutral density filter. All the measurements were conducted at room temperature.

Powder X-ray Diffraction Analysis: Room temperature powder XRD analysis was collected with a Bruker D8 Advance MKII diffractometer using Cu Kα radiation with divergent (Bragg-Brentano) geometries. The 2θ range was 5° to 50°, with a step size of 0.02° and a step rate of 10 s.

STEM-EDS Acquisition: STEM-EDS mapping was acquired using a Titan3 Themis (ThermoFisher) at the University of Leeds equipped with an ultrahigh brightness "X-FEG" electron source and a 4-quadrant "Super-X" (Bruker) silicon drift detector system for EDS, operated at 300 kV. STEM-EDS was carried out in conjunction with annular dark-field (ADF-STEM) imaging using a probe current of 82 pA. The acquisition time was 15 min for each STEM-EDS spectrum image.

CL-EDS Correlation: STEM-CL and STEM-EDS signals were correlated by first identifying the relative orientation of the two spectrum image datasets. LHP grain shape and relative position were used to identify the relative orientation of the two datasets in the overlay. Next, the local registration of CL emission and the ADF-STEM image simultaneously acquired with the STEM-EDS was refined for selected grains showing variable emission peaks between ≈620 and 660 nm. Local refinement was carried out to remove the effects of any residual scan or image distortions in either instrument used for STEM-CL or STEM-EDS, as well as to localize the brightest emission points observed in STEM-CL with individual grains observed in ADF-STEM during STEM-EDS acquisition.

$$\sigma_x = \sqrt{\left(\frac{1}{n_1}\right)^2 \sigma_{Br}^2 + \left(\frac{n_{Br}}{n_1^2}\right)^2 \sigma_1^2} \tag{1}$$

STEM-CL and STEM-EDS spectra were extracted from correlated features using HyperSpy, an open-source Python package for hyperspectral microscopy data. To avoid contributions from overlapping grains and to minimize the effects of surrounding matrix material, the spectra were extracted from areas of grains showing bright CL and minimal overlap in ADF-STEM. STEM-EDS spectra were integrated into a window at the Br Lα (1.39 to 1.6 keV) and a window at the I Lα (3.82 to 4.06 keV) X-ray emission peaks, defined based on the full, non-overlapping peak widths in the sum spectrum for the entire spectrum image. Uncertainties in the integrated counts n were taken as $\sigma = \sqrt{n}$ given the predominant Poisson noise contribution in STEM-EDS. The error in the ratio was determined from error propagation according to

$$x = \frac{n_{Br}}{n_1} \tag{2}$$

STEM-EDS were normalized setting the Cs Lα peak to 1 for plotting. STEM-CL spectra were likewise normalized by setting the maximum intensity to 1 for plotting. Single-pixel spectra from STEM-CL were rebinned in wavelength by a factor of 4 and STEM-EDS spectra were rebinned in energy by a factor of 8 for visualization. Rebinned STEM-CL spectra were then fitted with a Gaussian function in Origin at the highest intensity peak in the spectrum to extract the peak center in nm. Uncertainties in the wavelength for the emission peak were taken as the standard error in the fit for the center parameter of the Gaussian. Finally, the extracted peak centers were plotted as a function of the ratio of integrated intensities (Br Lα)/(I Lα). Values less than 1 exhibit greater contributions from I Lα whereas a de-

fined Br Lα was visible in spectra with ratios approximately equal to or exceeding 1.

Cathodoluminescence in a STEM: STEM imaging and CL spectroscopy were performed on a modified Nion Hermes200 operated with 100 keV kinetic energy electrons. With this microscope, a subnanometer electron beam can be generated for high spatial resolution imaging and spectroscopy. High-angle annular dark field (HAADF) images had an intensity that was proportional to the projected atomic number along the electron beam trajectory. Therefore, the heavier CsPbI$_3$ particles appeared brighter in the lighter MOF. CL was performed with a Mönch system from Attolight fitted with a diffraction grating 150 grouves per millimeter (0.34 nm dispersion on the spectrometer used), which gave an energy wavelength resolution of about 1 nm at 600 nm. The optical spectrometer was calibrated using an Ar–Hg lamp. The sample was kept at around 150 K using a liquid nitrogen-cooled sample holder (HennyZ).

Scanning Electron Microscopy: The surface morphologies and atomic density information near the surface were investigated with a high-resolution SEM JEOL JSM-7100F, under both secondary electron and backscattered mode (15 kV acceleration voltage). All samples were dried in a vacuum oven followed by carbon coating prior to the imaging.

Synchrotron Tera-Hz Far-Infrared Absorption Spectroscopy: THz/Far-IR absorption spectra were collected at the THz/Far-IR beamline at the Australian Synchrotron with a Bruker IFS 125/HR Fourier transform (FT) spectrometer. The bolometer was kept under a cryogenic condition with liquid helium to improve the signal-to-noise ratio, and a 6 µm thick Multilayer Mylar beam splitter was used. For the measurement, attenuated total reflection (ATR) was applied. Samples were mounted on the surface of the diamond crystal window and held in position by applied pressure. Temperature-resolved in situ spectra were collected with the ATR heating stage and the sample was kept under flowing Ar ($\approx$20 mL min^{-1}). For data processing, the extended ATR correction algorithms in the OPUS 8.0 software, together with NumPy module v1.15 together with Python v3.5, were applied for spectral data correction and peak fitting.[40]

Computational Details: Density functional theory (DFT)-based first-principles calculations were carried out using the Vienna ab initio simulation package (VASP)[41] within the Perdew–Burke–Ernzerhof (PBE) of generalized gradient approximation (GGA) functional.[42] The electron-ion correlation was described by the projector augmented-wave (PAW) method.[43] To simulate the structure of the CsPbI$_x$Br$_{3-x}$ crystal, the I in the CsPdI$_3$ bulk was randomly replaced with Br and fully optimized the final structure. The kinetic cut-off energy was 500 eV, while the reciprocal k-mesh was sampled by 3 × 3 × 1 Monkhorst–Pack grids for the surface of CsPbI$_x$Br$_{3-x}$. A vacuum layer of over 30 Å was adopted to avoid the periodic structural interactions, and the DFT-D3 method[44] was used to correct the van der Waals interaction. The structures were relaxed under the fixation of the bottom four atomic layers within the criterion of 10^{-4} eV Å^{-1} and 0.01 eV for force and energy on each atom in the top layers, respectively. Five types of defects were considered in this calculation, including the I/Br vacancy, the Pb vacancy, I/Br$_i$ interstitials, and I/Br$_{Pb}$ and Pb$_{I/Br}$ antisite defects. The a$_g$ZIF was simulated with a ZIF-62 crystal structure. To reduce the computational cost, the ZIF-62 structures were separated into two different groups with Zn- or imidazole-terminations based on the repeated Zn-imidazole unit in the ZIF-62 framework.

The interaction energy (E_i) for gas molecules adsorption was estimated by

$$E_i = E_{total} - E_{Sub} - E_{ZIF} \tag{3}$$

where E_{total} and E_{Sub} represent the total energies of the PdI$_x$Br$_{2-x}$-terminated surface with and without ZIF-62 adsorption. E_{ZIF} is the energy for the groups with Zn- or imidazole-termination. The charge density difference ($\Delta\rho$) was calculated by

$$\Delta\rho = \rho_{total} - \rho_{Sub} - \rho_{ZIF} \tag{4}$$

where ρ_{total}, ρ_{Sub}, and ρ_{gas} are the charge density for the ZIF-62 adsorbed PbI$_x$Br$_{2-x}$-terminated surface, pure PbI$_x$Br$_{2-x}$-terminated surface, and the groups with Zn- or imidazole-termination, respectively.

Supporting Information

Acknowledgements

Conflict of Interest

The authors declare no conflict of interest.

Data Availability Statement

The data that support the findings of this study are available from the corresponding author upon reasonable request.

Keywords

[1] a) K. Frohna, M. Anaya, S. Macpherson, J. Sung, T. A. S. Doherty, Y.-H. Chiang, A. J. Winchester, K. W. P. Orr, J. E. Parker, P. D. Quinn, K. M. Dani, A. Rao, S. D. Stranks, *Nat. Nanotechnol.* **2022**, *17*, 190; b) T. A. S. Doherty, A. J. Winchester, S. Macpherson, D. N. Johnstone, V. Pareek, E. M. Tennyson, S. Kosar, F. U. Kosasih, M. Anaya, M. Abdi-Jalebi, Z. Andaji-Garmaroudi, E. L. Wong, J. Madéo, Y.-H. Chiang, J.-S. Park, Y.-K. Jung, C. E. Petoukhoff, G. Divitini, M. K. L. Man, C. Ducati, A. Walsh, P. A. Midgley, K. M. Dani, S. D. Stranks, *Nature* **2020**, *580*, 360.

[2] a) M. Saliba, T. Matsui, J.-Y. Seo, K. Domanski, J.-P. Correa-Baena, M. K. Nazeeruddin, S. M. Zakeeruddin, W. Tress, A. Abate, A. Hagfeldt, *Energy Environ. Sci.* **2016**, *9*, 1989; b) G. E. Eperon, S. D. Stranks, C. Menelaou, M. B. Johnston, L. M. Herz, H. J. Snaith, *Energy Environ. Sci.* **2014**, *7*, 982; c) A. Sadhanala, S. Ahmad, B. Zhao, N. Giesbrecht, P. M. Pearce, F. Deschler, R. L. Hoye, K. C. Gödel, T. Bein, P. Docampo, *Nano Lett.* **2015**, *15*, 6095; d) L. Sun, W. Li, W. Zhu, Z. Chen, *J. Mater. Chem. C* **2020**, *8*, 11664.

[3] a) H. Min, M. Kim, S.-U. Lee, H. Kim, G. Kim, K. Choi, J. H. Lee, S. I. Seok, *Science* **2019**, *366*, 749; b) D. Bi, W. Tress, M. I. Dar, P. Gao, J. Luo, C. Renevier, K. Schenk, A. Abate, F. Giordano, J.-P. C. Baena, *Sci. Adv.* **2016**, *2*, e1501170; c) F. Hao, C. C. Stoumpos, R. P. Chang, M. G. Kanatzidis, *J. Am. Chem. Soc.* **2014**, *136*, 8094.

[4] a) Y. Ogomi, A. Morita, S. Tsukamoto, T. Saitho, N. Fujikawa, Q. Shen, T. Toyoda, K. Yoshino, S. S. Pandey, T. Ma, *J. Phys. Chem. Lett.* **2014**, *5*, 1004; b) M. Ghasemi, L. Zhang, J. H. Yun, M. Hao, D. He, P. Chen, Y. Bai, T. Lin, M. Xiao, A. Du, *Adv. Funct. Mater.* **2020**, *30*, 2002342; c) M. Lyu, J.-H. Yun, M. Cai, Y. Jiao, P. V. Bernhardt, M. Zhang, Q. Wang, A. Du, H. Wang, G. Liu, L. Wang, *Nano Res.* **2016**, *9*, 692; d) M. Ghasemi, M. Q. Lyu, M. Roknuzzaman, J. H. Yun, M. M. Hao, D. X. He, Y. Bai, P. Chen, P. V. Bernhardt, K. Ostrikov, L. Z. Wang, *J. Mater. Chem. A* **2019**, *7*, 20733.

[5] a) J. H. Noh, S. H. Im, J. H. Heo, T. N. Mandal, S. I. Seok, *Nano Lett.* **2013**, *13*, 1764; b) C. M. Sutter-Fella, Y. Li, M. Amani, J. W. Ager III, F. M. Toma, E. Yablonovitch, I. D. Sharp, A. Javey, *Nano Lett.* **2016**, *16*, 800.

[6] a) J. Xu, C. C. Boyd, J. Y. Zhengshan, A. F. Palmstrom, D. J. Witter, B. W. Larson, R. M. France, J. Werner, S. P. Harvey, E. J. Wolf, *Science* **2020**, *367*, 1097; b) L. K. Ono, E. J. Juarez-Perez, Y. Qi, *ACS Appl. Mater. Interfaces* **2017**, *9*, 30197.

[7] M. R. Filip, G. E. Eperon, H. J. Snaith, F. Giustino, *Nat. Commun.* **2014**, *5*, 5757.

[8] a) D. P. McMeekin, G. Sadoughi, W. Rehman, G. E. Eperon, M. Saliba, M. T. Hörantner, A. Haghighirad, N. Sakai, L. Korte, B. Rech, *Science* **2016**, *351*, 151; b) Z. Xiao, L. Zhao, N. L. Tran, Y. L. Lin, S. H. Silver, R. A. Kerner, N. Yao, A. Kahn, G. D. Scholes, B. P. Rand, *Nano Lett.* **2017**, *17*, 6863; c) G. Xing, N. Mathews, S. S. Lim, N. Yantara, X. Liu, D. Sabba, M. Grätzel, S. Mhaisalkar, T. C. Sum, *Nat. Mater.* **2014**, *13*, 476.

[9] E. T. Hoke, D. J. Slotcavage, E. R. Dohner, A. R. Bowring, H. I. Karunadasa, M. D. McGehee, *Chem. Sci.* **2015**, *6*, 613.

[10] a) D. J. Slotcavage, H. I. Karunadasa, M. D. McGehee, *ACS Energy Lett.* **2016**, *1*, 1199; b) S. J. Yoon, S. Draguta, J. S. Manser, O. Sharia, W. F. Schneider, M. Kuno, P. V. Kamat, *ACS Energy Lett.* **2016**, *1*, 290; c) S. Draguta, O. Sharia, S. J. Yoon, M. C. Brennan, Y. V. Morozov, J. S. Manser, P. V. Kamat, W. F. Schneider, M. Kuno, *Nat. Commun.* **2017**, *8*, 200; d) S. J. Yoon, M. Kuno, P. V. Kamat, *ACS Energy Lett.* **2017**, *2*, 1507; e) M. C. Brennan, S. Draguta, P. V. Kamat, M. Kuno, *ACS Energy Lett.* **2017**, *3*, 204.

[11] E. Unger, L. Kegelmann, K. Suchan, D. Sörell, L. Korte, S. Albrecht, *J. Mater. Chem. A* **2017**, *5*, 11401.

[12] D. Guo, Z. Andaji Garmaroudi, M. Abdi-Jalebi, S. D. Stranks, T. J. Savenije, *ACS Energy Lett.* **2019**, *4*, 2360.

[13] A. J. Barker, A. Sadhanala, F. Deschler, M. Gandini, S. P. Senanayak, P. M. Pearce, E. Mosconi, A. J. Pearson, Y. Wu, A. R. Srimath Kandada, T. Leijtens, F. De Angelis, S. E. Dutton, A. Petrozza, R. H. Friend, *ACS Energy Lett.* **2017**, *2*, 1416.

[14] a) M. Abdi-Jalebi, Z. Andaji-Garmaroudi, S. Cacovich, C. Stavrakas, B. Philippe, J. M. Richter, M. Alsari, E. P. Booker, E. M. Hutter, A. J. Pearson, *Nature* **2018**, *555*, 497; b) Y. Zhou, Y. H. Jia, H. H. Fang, M. A. Loi, F. Y. Xie, L. Gong, M. C. Qin, X. H. Lu, C. P. Wong, N. Zhao, *Adv. Funct. Mater.* **2018**, *28*, 1803130.

[15] A. s. F. Gualdrón-Reyes, S. J. Yoon, E. M. Barea, S. Agouram, V. Muñoz-Sanjosé, A. n. M. Meléndez, M. E. Niño-Gómez, i. n. Mora-Seró, *ACS Energy Lett.* **2018**, *4*, 54.

[16] a) J. Luo, W. Zhang, H. Yang, Q. Fan, F. Xiong, S. Liu, D. S. Li, B. Liu, *EcoMat* **2021**, *3*, e12079; b) X. Xu, Y. Pan, L. Ge, Y. Chen, X. Mao, D. Guan, M. Li, Y. Zhong, Z. Hu, V. K. Peterson, M. Saunders, C. T. Chen, H. Zhang, R. Ran, A. Du, H. Wang, S. P. Jiang, W. Zhou, Z. Shao, *Small* **2021**, *17*, 2101573; c) T. H. Han, J. W. Lee, C. Choi, S. Tan, C. Lee, Y. Zhao, Z. Dai, N. De Marco, S. J. Lee, S. H. Bae, Y. Yuan, H. M. Lee, Y. Huang, Y. Yang, *Nat. Commun.* **2019**, *10*, 520; d) P. Wang, B. Wang,

2304236 (11 of 12)

Y. Liu, L. Li, H. Zhao, Y. Chen, J. Li, S. F. Liu, K. Zhao, *Angew. Chem., Int. Ed. Engl.* **2020**, *59*, 23100; e) D. T. Ke Sun, X. Fang, X. Xia, D. Lin, J. Song, Y. Lin, Z. Liu, M. Gu, Y. Yue, J. Qiu, *Science* **2022**, *375*, 307.

[17] a) L. Borchardt, Q.-L. Zhu, M. E. Casco, R. Berger, X. Zhuang, S. Kaskel, X. Feng, Q. Xu, *Mater. Today* **2017**, *20*, 592; b) Y. Cui, B. Li, H. He, W. Zhou, B. Chen, G. Qian, *Acc. Chem. Res.* **2016**, *49*, 483.

[18] J. Ren, T. Li, X. Zhou, X. Dong, A. V. Shorokhov, M. B. Semenov, V. D. Krevchik, Y. Wang, *Chem. Eng. J.* **2019**, *358*, 30.

[19] J. Hou, P. Chen, A. Shukla, A. Krajnc, T. Wang, X. Li, R. Doasa, L. H. Tizei, B. Chan, D. N. Johnstone, *Science* **2021**, *374*, 621.

[20] T. D. Bennett, Y. Yue, P. Li, A. Qiao, H. Tao, N. G. Greaves, T. Richards, G. I. Lampronti, S. A. Redfern, F. d. r. Blanc, *J. Am. Chem. Soc.* **2016**, *138*, 3484.

[21] J. Hou, C. W. Ashling, S. M. Collins, A. Krajnc, C. Zhou, L. Longley, D. N. Johnstone, P. A. Chater, S. Li, M.-V. Coulet, *Nat. Commun.* **2019**, *10*, 2580.

[22] Q. Zhang, Y. Zhou, Y. Wei, M. Tai, H. Nan, Y. Gu, J. Han, X. Yin, J. Li, H. Lin, *J. Mater. Chem. C* **2020**, *8*, 2569.

[23] X. He, Y. Qiu, S. Yang, *Adv. Mater.* **2017**, *29*, 1700775.

[24] A. Swarnkar, A. R. Marshall, E. M. Sanehira, B. D. Chernomordik, D. T. Moore, J. A. Christians, T. Chakrabarti, J. M. Luther, *Science* **2016**, *354*, 92.

[25] Y.-H. Kim, S. Kim, A. Kakekhani, J. Park, J. Park, Y.-H. Lee, H. Xu, S. Nagane, R. B. Wexler, D.-H. Kim, *Nat. Photonics* **2021**, *15*, 148.

[26] J. Lu, W. Chen, C. Zhou, S. Yang, C. Wang, R. Wang, X. Wang, Z. Gan, B. Jia, X. Wen, *J. Mater. Chem. C* **2021**, *9*, 8966.

[27] T. Schmidt, K. Lischka, W. Zulehner, *Phys. Rev. B* **1992**, *45*, 8989.

[28] N. Ben Sedrine, J. Esteves, J. Rodrigues, L. Rino, M. Correia, M. Sequeira, A. Neves, E. Alves, M. Bockowski, P. Edwards, *Sci. Rep.* **2015**, *5*, 13739.

[29] a) D. Ma, X. Rong, X. Zheng, W. Wang, P. Wang, T. Schulz, M. Albrecht, S. Metzner, M. Müller, O. August, *Sci. Rep.* **2017**, *7*, 46420; b) S. Draguta, S. Thakur, Y. V. Morozov, Y. Wang, J. S. Manser, P. V. Kamat, M. Kuno, *J. Phys. Chem. Lett.* **2016**, *7*, 715.

[30] R. E. Beal, D. J. Slotcavage, T. Leijtens, A. R. Bowring, R. A. Belisle, W. H. Nguyen, G. F. Burkhard, E. T. Hoke, M. D. McGehee, *J. Phys. Chem. Lett.* **2016**, *7*, 746.

[31] C. G. Bischak, C. L. Hetherington, H. Wu, S. Aloni, D. F. Ogletree, D. T. Limmer, N. S. Ginsberg, *Nano Lett.* **2017**, *17*, 1028.

[32] X. Wang, Y. Ling, X. Lian, Y. Xin, K. B. Dhungana, F. Perez-Orive, J. Knox, Z. Chen, Y. Zhou, D. Beery, *Nat. Commun.* **2019**, *10*, 695.

[33] a) C. Eames, J. M. Frost, P. R. Barnes, B. C. O'regan, A. Walsh, M. S. Islam, *Nat. Commun.* **2015**, *6*, 7497; b) W. Chen, W. Li, Z. Gan, Y.-B. Cheng, B. Jia, X. Wen, *Chem. Mater.* **2019**, *31*, 9049.

[34] L. Hu, X. Guan, W. Chen, Y. Yao, T. Wan, C.-H. Lin, N. D. Pham, L. Yuan, X. Geng, F. Wang, *ACS Energy Lett.* **2021**, *6*, 1649.

[35] a) D. W. DeQuilettes, W. Zhang, V. M. Burlakov, D. J. Graham, T. Leijtens, A. Osherov, V. Bulović, H. J. Snaith, D. S. Ginger, S. D. Stranks, *Nat. Commun.* **2016**, *7*, 11683; b) Y. Shao, Y. Fang, T. Li, Q. Wang, Q. Dong, Y. Deng, Y. Yuan, H. Wei, M. Wang, A. Gruverman, J. Shield, J. Huang, *Energy Environ. Sci.* **2016**, *9*, 1752; c) Y. Wang, Z. Hu, C. Gao, C. Yang, J. Zhang, Y. Zhu, *Adv. Mater. Interfaces* **2020**, *7*, 1901521; d) X. Deng, X. Wen, J. Zheng, T. Young, C. F. J. Lau, J. Kim, M. Green, S. Huang, A. Ho-Baillie, *Nano Energy* **2018**, *46*, 356.

[36] W. Li, M. U. Rothmann, A. Liu, Z. Wang, Y. Zhang, A. R. Pascoe, J. Lu, L. Jiang, Y. Chen, F. Huang, *Adv. Energy Mater.* **2017**, *7*, 1700946.

[37] A. Ruth, M. C. Brennan, S. Draguta, Y. V. Morozov, M. Zhukovskyi, B. Janko, P. Zapol, M. Kuno, *ACS Energy Lett.* **2018**, *3*, 2321.

[38] L. Frentzel-Beyme, M. Kloß, P. Kolodzeiski, R. Pallach, S. Henke, *J. Am. Chem. Soc.* **2019**, *141*, 12362.

[39] J. Hou, P. Chen, A. Shukla, A. Krajnc, T. Wang, X. Li, R. Doasa, L. H. G. Tizei, B. Chan, D. N. Johnstone, R. Lin, T. U. Schülli, I. Martens, D. Appadoo, M. S' Ari, Z. Wang, T. Wei, S.-C. Lo, M. Lu, S. Li, E. B. Namdas, G. Mali, A. K. Cheetham, S. M. Collins, V. Chen, L. Wang, T. D. Bennett, *Science* **2021**, *374*, 621.

[40] S. Van Der Walt, S. C. Colbert, G. Varoquaux, *Comput. Sci. Eng.* **2011**, *13*, 22.

[41] a) G. Kresse, J. Furthmüller, *Phys. Rev. B* **1996**, *54*, 11169; b) G. Kresse, J. Furthmüller, *Comput. Mater. Sci.* **1996**, *6*, 15.

[42] J. P. Perdew, K. Burke, M. Ernzerhof, *Phys. Rev. Lett.* **1996**, *77*, 3865.

[43] G. Kresse, D. Joubert, *Phys. Rev. B* **1999**, *59*, 1758.

[44] S. Grimme, J. Antony, S. Ehrlich, H. Krieg, *J. Chem. Phys.* **2010**, *132*, 154104.